Appendix of "A physics-guided smoothing method for material modeling with digital image correlation measurements"

1 Constitutive Law Learning

Instead of learning a PDE solution operator which maps from a body load function $\mathbf{b}$ to the desired solution (displacement) field $\mathbf{u}$, constitutive operator learning approaches [6] aim to construct a surrogate operator $\mathcal{G}: \mathbb{U} \to \mathbb{F}$ that maps from the displacement function $\mathbf{u}(\mathbf{x})$ to the body load function $\mathbf{b}(\mathbf{x})$. Without loss of generality, in this work we consider the constitutive operator as a peridynamic material model. For simplicity, we focus on (quasi)static and two-dimensional tasks.

1.1 Peridynamic Theory

Peridynamics is a continuum mechanics model, where the constitutive operator is written as an integral instead of differential operators as in classical PDEs. A quasi-static peridynamics model writes:

$$\int_{B_\delta(\mathbf{x})} \mathbf{f}(\mathbf{u},\mathbf{q},\mathbf{x})\, d\mathbf{q} + \mathbf{b}(\mathbf{x}) = \mathbf{0}, \quad \mathbf{x} \in \Omega, \tag{13}$$

where $\Omega \subset \mathbb{R}^d$ is a domain of interest, $\mathbf{x}$ and $\mathbf{q}$ are material points in the reference (undeformed) configuration of the body. $B_\delta(\mathbf{x})$ is a ball centered at $\mathbf{x}$ of radius δ. $\mathbf{u}$ is the displacement field, $\mathbf{b}(\mathbf{x},t)$ is the body force density (external loading). $\mathbf{f}(\mathbf{u},\mathbf{q},\mathbf{x})$ is the pairwise bond force density that $\mathbf{q}$ exerts on $\mathbf{x}$, satisfying $\mathbf{f}(\mathbf{u},\mathbf{q},\mathbf{x}) = -\mathbf{f}(\mathbf{u},\mathbf{x},\mathbf{q})$. The pairwise bond force density is given by

$$\mathbf{f}(\mathbf{u},\mathbf{q},\mathbf{x}) = \underline{\boldsymbol{T}}[\mathbf{u},\mathbf{x}]\langle \mathbf{q}-\mathbf{x}\rangle - \underline{\boldsymbol{T}}[\mathbf{u},\mathbf{q}]\langle \mathbf{x}-\mathbf{q}\rangle\,, \tag{14}$$

where the underlined symbols denote states. A material model $\hat{\underline{\boldsymbol{T}}}(\underline{\boldsymbol{Y}})$ determines the force state $\underline{\boldsymbol{T}}$ based on the deformation state $\underline{\boldsymbol{Y}}$, which is characterized by

$$\underline{\boldsymbol{Y}}[\mathbf{u},\mathbf{x}]\langle \mathbf{q}-\mathbf{x}\rangle = \boldsymbol{\xi} + \boldsymbol{\eta}, \text{ where } \boldsymbol{\xi} := \mathbf{q}-\mathbf{x},\ \boldsymbol{\eta} := \mathbf{u}(\mathbf{q}) - \mathbf{u}(\mathbf{x}). \tag{15}$$

Denoting the unit direction of the deformed bond as:

$$\underline{\boldsymbol{D}}[\mathbf{u},\mathbf{x}]\langle \mathbf{q}-\mathbf{x}\rangle := \frac{\underline{\boldsymbol{Y}}[\mathbf{u},\mathbf{x}]\langle \mathbf{q}-\mathbf{x}\rangle}{\left|\underline{\boldsymbol{Y}}[\mathbf{u},\mathbf{x},t]\langle \mathbf{q}-\mathbf{x}\rangle\right|} = \frac{\boldsymbol{\xi}+\boldsymbol{\eta}}{|\boldsymbol{\xi}+\boldsymbol{\eta}|}, \tag{16}$$

and the length changes of the bond as

$$\underline{e}[\mathbf{u},\mathbf{x}]\langle \mathbf{q}-\mathbf{x}\rangle := |\boldsymbol{\xi}+\boldsymbol{\eta}| - |\boldsymbol{\xi}|, \tag{17}$$

then the material model for a heterogeneous body composed of ordinary, mobile material can be written as:

$$\hat{\underline{\boldsymbol{T}}}(\underline{\boldsymbol{Y}},\mathbf{x}) = \underline{t}(\underline{e},\mathbf{x})\,\underline{\boldsymbol{D}}\,, \tag{18}$$

where $\underline{t}$ denotes the scalar force state. This formulation guarantees linear and angular momentum conservation, Galilean invariance, and frame invariance (objectivity).
Then we obtain the peridynamic model:

$$\mathcal{G}[\mathbf{u}](\mathbf{x}) + \mathbf{b}(\mathbf{x}) = \mathbf{0}, \text{ for } \mathbf{x} \in \Omega, \tag{19}$$

where the operator $\mathcal{G}$ is formulated as:

$$\mathcal{G}[\mathbf{u}](\mathbf{x}) := \int_{B_\delta(\mathbf{0})} \left(\underline{t}[\mathbf{u},\mathbf{x}]\langle \boldsymbol{\xi}\rangle + \underline{t}[\mathbf{u},\mathbf{x}+\boldsymbol{\xi}]\langle -\boldsymbol{\xi}\rangle\right) \underline{\boldsymbol{D}}[\mathbf{u},\mathbf{x}]\langle \boldsymbol{\xi}\rangle\, d\boldsymbol{\xi}, \tag{20}$$

with boundary conditions are supplied by

$$\mathbf{u}(\mathbf{x}) = \mathbf{u}_{BC}(\mathbf{x}), \text{ for } \mathbf{x} \in \Omega_I, \tag{21}$$

where $\Omega_I := \{\mathbf{x} | \mathbf{x} \in \mathbb{R}^d \backslash \Omega, \text{dist}(\mathbf{x},\Omega) < 2\delta\}$ is the interaction region in which boundary data $\mathbf{u}_{BC}$ is prescribed.

1.2 Peridynamics operator learning (PNO)

To learn a constitutive operator based on peridynamic theory, one can parameterize the scalar force state $\underline{t}$ with neural networks:

$$\underline{t}[\mathbf{u},\mathbf{x}]\langle\boldsymbol{\xi}\rangle := t^{NN}(\omega(\mathbf{x},\boldsymbol{\xi}),\vartheta(\mathbf{x}),\underline{e}[\mathbf{u},\mathbf{x}]\langle\boldsymbol{\xi}\rangle,|\boldsymbol{\xi}|;\mathbf{v}) \,, \tag{22}$$

where

$$\omega(\mathbf{x},\boldsymbol{\xi}) := \omega^{NN}(\boldsymbol{R}(-\alpha(\mathbf{x}))\boldsymbol{\xi};\mathbf{w}) \,, \tag{23}$$

$$\boldsymbol{R}(\theta) := \begin{bmatrix}\cos\theta & -\sin\theta\\ \sin\theta & \cos\theta\end{bmatrix}, \tag{24}$$

$$\vartheta(\mathbf{x}) := \frac{\int_{B_\delta(\mathbf{0})}\omega^{NN}(\boldsymbol{\xi};\mathbf{w})\,\underline{e}[\mathbf{u},\mathbf{x}]\langle\boldsymbol{\xi}\rangle|\boldsymbol{\xi}|d\boldsymbol{\xi}}{\int_{B_\delta(\mathbf{0})}\omega^{NN}(\boldsymbol{\xi};\mathbf{w})\,|\boldsymbol{\xi}|^2 d\boldsymbol{\xi}} \,. \tag{25}$$

Here, t^{NN} and ω^{NN} are scalar-valued functions implemented as multi-layer perceptrons (MLPs) with learnable parameters $\mathbf{v}$ and $\mathbf{w}$, respectively. The function ω serves as a kernel that defines the weighting of neighboring material points. To account for fiber orientation at each location, the rotation matrix $\boldsymbol{R}$ is introduced to capture the fiber orientation at each location by aligning the direction of the kernel function with the fiber orientation. If the material is homogeneous, then ω can only depend on the direction of the bond vector $\boldsymbol{\xi}$ as well as $|\boldsymbol{\xi}|$, i.e., $\omega(\mathbf{x},\boldsymbol{\xi}) := \omega(\boldsymbol{\xi})$. Here ϑ represents a nonlocal generalization of the dilatation, which describes the volume change of material near a point due to the deformation in volume.
With the PNO architecture, one can model complex material mechanical responses learned from data. In particular, given a set of function pair observations $\mathcal{D} = \{\mathbf{u}^s(\mathbf{x}),\mathbf{b}^s(\mathbf{x})\}_{s=1}^{S_{tr}}$ of the loading field $\mathbf{b}^s(\mathbf{x})$ and the corresponding displacement field $\mathbf{u}^s(\mathbf{x})$, the set of parameters in the network architecture is inferred by minimizing the error in (19).
When $\mathbf{b} \neq 0$, one can use the relative L^2 error of the output function, $\mathbf{b}$, as the loss function:

$$\text{loss}_{\mathbf{b}} = \frac{1}{S_{tr}}\sum_{s=1}^{S_{tr}}\frac{||\mathcal{G}[\mathbf{u}^s]+\mathbf{b}^s||_{L^2(\Omega)}}{||\mathbf{b}^s||_{L^2(\Omega)}} \,. \tag{26}$$

However, in biaxial testing protocols we are considering here, external forces are absent. Then, the loss function (26) becomes invalid due to a zero denominator. To overcome this issue, we reformulate the loss function using the displacement field and the averaged axial components of the first Piola–Kirchhoff stress:

$$\text{loss} = \frac{\gamma}{S_{tr}}\sum_{s=1}^{S_{tr}}\frac{\left\|\mathcal{G}^{-1}[\mathbf{b}^s]+\mathbf{u}^s\right\|_{L^2(\Omega)}}{||\mathbf{u}^s||_{L^2(\Omega)}} + \frac{1-\gamma}{S_{tr}}\sum_{s=1}^{S_{tr}}\frac{\left|\mathbf{P}^s_{exp}-\mathbf{P}^s\right|}{\bar{\mathbf{P}}} \,, \tag{27}$$

where $\mathbf{P}^s_{exp}$ denotes the spatial average of axial first Piola–Kirchhoff stresses for sample s, and $\bar{\mathbf{P}}$ is the mean of axial ground truth stresses across all training samples, γ is a tunable hyperparameter. Once the constitutive law is obtained, for any new loading instance $\mathbf{b}(\mathbf{x})$, we solve for the displacement field $\mathbf{u}(\mathbf{x})$ using an iterative nonlinear static solver. Hence, the PNO model is generalizable to new and unseen loading instances.

2 DIC Datasets

Traditional strain gauges, working well for engineering materials (e.g., aluminum/steel), are not capable of measuring the strain of biological tissues typically under a large deformation regime. On the other hand, laser or optical extensometer are the experimental alternative to measure large-deformation strains of bio-tissues, but they are limited to 1D axial strain measurements. Since most of the soft bio-tissues are highly nonlinear and heterogeneous in nature, digital image correlation (DIC) is a more commonly adopted displacement- and strain-tracking technique that can be integrated with the planar biaxial testing system – our application focus.

2.1 Data Collection for dataset 1

This dataset is generated from a biaxial testing on a standard nitrile glove sourced from Dealmed (New York, USA), cutting a 7.5 mm by 7.5 mm specimen for analysis. The specimen's thickness was precisely measured using a Keyence laser thickness gauge (Illinois, USA). We then applied a random speckle pattern to the surface using an airbrush.
The speckled specimen was mounted on a biaxial testing device from CellScale Biomaterials Testing Co. (Canada), using five BioRake tines for secure fixation. During the biaxial testing, three loading-unloading cycles were performed in each direction,

with a target force of 750 mN. Force and actuator position data were recorded at 5 Hz for stress and strain calculations, essential for the constitutive model fitting.

Simultaneously, a CCD camera captured images at 5 Hz, and digital image correlation (DIC) analysis was conducted using the CellScale LabJoy software. The central 6 mm by 5.5 mm region of the specimen, which had a more uniformly distributed speckle pattern, was selected for tracking. A 20 by 20 node grid was constructed, and the tracked coordinates were exported for further analysis.

2.2 Data Collection for dataset 2

This dataset is from a biaxial mechanical testing on porcine tricuspid valve anterior leaflet (TVAL) tissue. The tissue was sourced from an adult porcine heart (120 kg, 1.5 years old) obtained from a USDA-approved abattoir. Upon arrival at the laboratory, the TVAL tissue was sectioned into square specimens, and thickness measurements were taken at three locations using an optical system, yielding an average tissue thickness of 0.22 mm. A random speckle pattern was applied to the surface of the tissue using black paint to facilitate displacement tracking via DIC, with fiducial markers added to ensure accurate measurements.

The prepared specimen was mounted on a biaxial testing system (BioTester, CellScale), with an effective testing area of 8.72 $\times$ 10.75 mm. Prior to mechanical testing, the specimen underwent preconditioning in phosphate-buffered saline (PBS) to mimic in vivo conditions, following a protocol of 10 cycles of equi-biaxial tension loading and unloading, aiming for a first Piola-Kirchhoff stress of 150 kPa.

Subsequent biaxial tension tests involved seven different loading protocols, each with different biaxial stress ratios ($P_{11} : P_{22}$), including combinations of 1:1, 1:0.75, 1:0.5, 1:0.25, 0.75:1, 0.5:1, and 0.25:1. Each protocol was repeated for five cycles of loading and unloading, with force and actuator position data recorded at a frequency of 5 Hz, resulting in a total of 1926 data points.

To minimize stress concentration effects near the mounting hooks, deformation analysis focused on the central region of the specimen (4.4 $\times$ 4.4 mm). The force-displacement data were smooth, thanks to the high-resolution load cell with 0.1% accuracy. The displacement rates used during testing (0.16 mm/s in the X-direction and 0.28 mm/s in the Y-direction) were low enough to avoid significant viscoelastic effects, ensuring the tests were quasi-static with minimal hysteresis. This approach allowed for reliable mechanical characterization of the tissue's biaxial behavior under the given conditions.

3 Experimental Details

3.1 Details in PGS implementation

In the PGS implementation, we set the maximum number of iterations to 50,000. The initial learning rate is 1e-5, with a learning rate decay factor of 0.9 applied every 1,000 steps. The basis function is a first-order polynomial. The training stopping criteria parameters $\mathrm{TOL}_{\mathbf{u}}$ and $\mathrm{TOL}_{\mathbf{E}}$ are set to 3 and 1e-5, respectively.

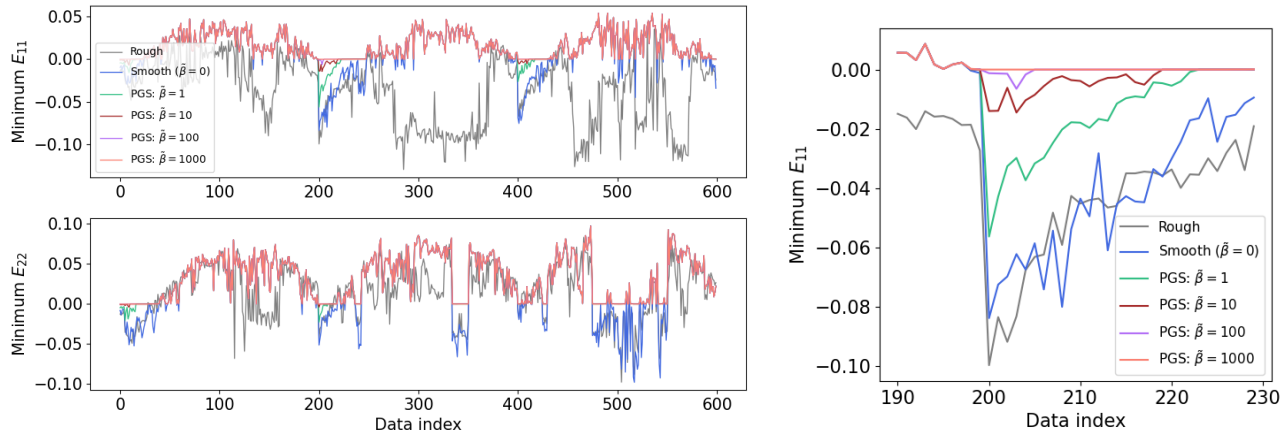

Fig. 6: Dataset 1: Comparison of strains of PGS data obtained using different $\tilde{\beta}$.

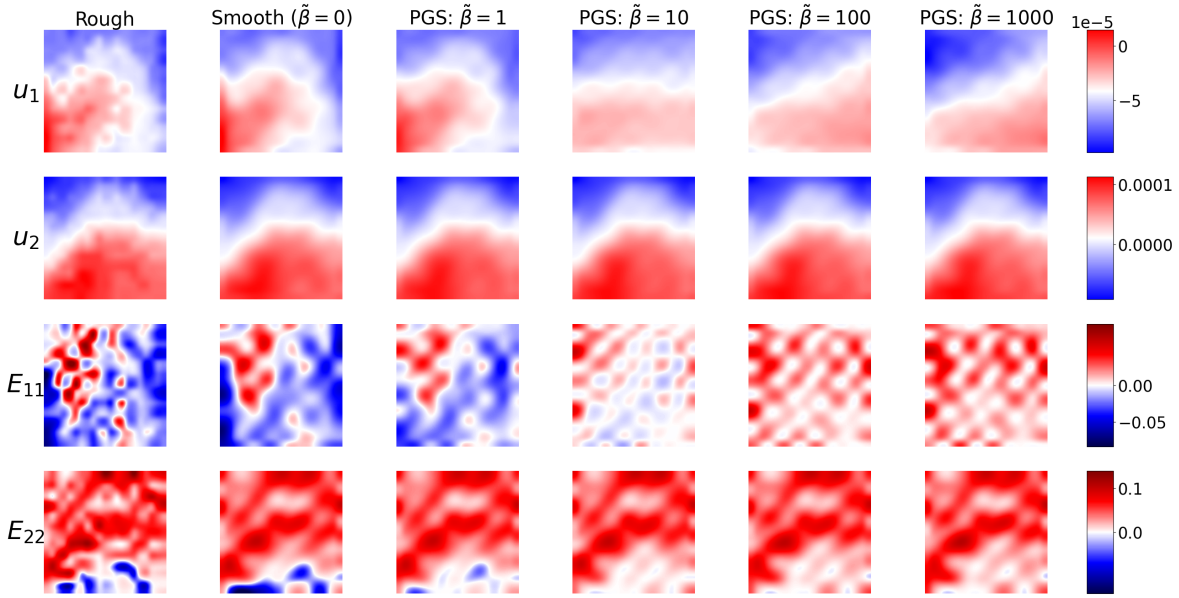

Fig. 7: Dataset 2: Comparison of the displacements and strains when using different weight parameters $\tilde{\beta}$.

3.2 Details in PNO training

The widths of the MLPs for ω^{NN}, t^{NN} and α^{NN} are (2, 256, 512, 1), (4, 512, 512, 1), and (2, 128, 128, 1) respectively, and the peridynamic horizon size is set as $\delta = 3\Delta x$. In all experiments we decrease the learning rate with a ratio of decay rate every 50 epochs. There are several different values of the initial learning rates and learning rate decay factors are considered to obtain the best training results on each dataset.

4 Additional Results

Herein, we provide more results as a supplement of Section 4.
As a supplement of the ablation study, in Fig. 6. we show the minimum strains when using different levels of physical loss parameter, $\tilde{\beta}$. It can be seen that when $\tilde{\beta}$ is too small (e.g., $\tilde{\beta} = 1$), the algorithm can not sufficiently eliminates all negative strains. When $\tilde{\beta}$ gets larger, the discrepancy between observed $\mathbf{u}_{exp}$ and the reconstructed $\mathbf{u}$ also increases. From Fig. 6 and 7, it looks like $\tilde{\beta} = 100$ provides a good balance between these two effects.
As a supplement of experiments for dataset 2, in Fig. 8 we demonstrate the reconstructed strain fields in an exemplar sample, from PGS and the two baselines. One can see that this dataset has smaller negative strain regimes, and PGS still successfully eliminates them without drastically changing the displacement field.

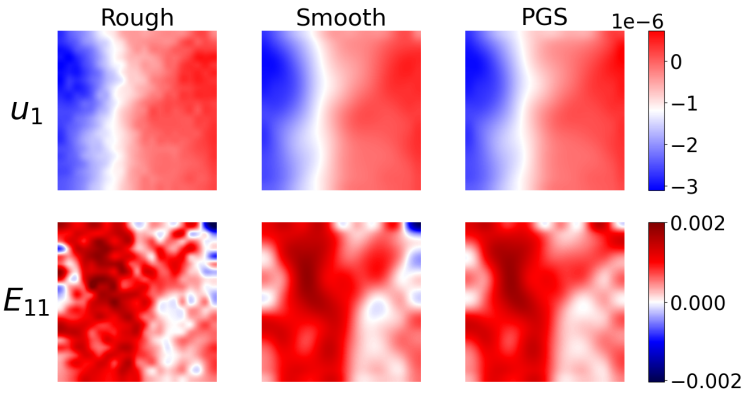

Fig. 8: Dataset 2: Comparison of displacement u_1 and strain ϵ_{11} from three datasets.